Tailoring the microstructure and the mechanical properties of ultrafine grained high strength ferritic steels by powder metallurgy

Bassem Mouawad, Xavier Boulnat, Damien Fabrègue, Michel Perez, Yann de Carlan

Tailoring the microstructure and the mechanical properties of ultrafine grained high strength ferritic steels by powder metallurgy

B. Mouawad [a], X. Boulnat [a, b], D. Fabrègue [a, *], M. Perez [a], Y. de Carlan [b]

[a] *Université de Lyon, INSA-Lyon, MATEIS UMR CNRS 5510, F69621 Villeurbanne, France*
[b] *CEA Saclay, DEN, Service de Recherches Métallurgiques Appliquées, F91191 Gif-sur-Yvette, France*

Three model powder materials (i) atomized, (ii) atomized + milled, and, (iii) atomized + milled + alloyed with yttria (Y_2O_3) and titanium were consolidated within Spark Plasma Sintering device at 850, 950 and 1050°C. Depending on the materials, nanostructured, or even bimodal grain size distribution can be observed. These structures lead to a wide range of mechanical behavior: the tensile strength at room temperature can be tailored from 500 to 1200 MPa with total elongation from 8 to 35%.

The bimodal grain size distribution is believed to provide both good yield stress and ductility. Finally, a yield stress model based on the effect of solute atoms, dislocations, grains boundaries and precipitates is presented and it permits to predict accurately the experimental values for all specimens and conditions.

1. Introduction

The viability of improved nuclear concepts such as sodium fast neutron reactors depends on the development of high-performance structural materials that can support aggressive environments and high neutron flux. Oxide-Dispersion Strengthened (ODS) ferritic steels that exhibit limited irradiation swelling and excellent creep properties are being developed by powder metallurgy, well-known to produce nanostructured and ultrafine grained materials [1–3]. ODS ferritic steels are high strength materials thanks to a specific dispersion of fine oxides within the ferritic matrix [4–10].

To do so, the fabrication route includes a milling step where micrometric Yttria powder and pre-alloyed ferritic powder are mechanically alloyed. Then, Hot Isostatic Pressing (HIP) and/or Hot Extrusion (HE) are classic steps to consolidate the materials [11]. However, significant grain growth is often observed since these processes require exposure for hours at high temperature (T > 1000°C) [12–14]. Compared to HIP, Spark Plasma Sintering (SPS) necessitates much less time in both heating and cooling during sintering process [15]. SPS has been widely used because of its ability to heat up the material very quickly, providing a powerful tool to retain the original nanostructure [16–19]. For industrial purpose, it has been used for ceramics applications and refractory materials whereas only few studies were dedicated to metallic materials [20,21]. Ji et al. [17,22] demonstrated that SPS can be used to retain the nanostructure of ODS intermetallic alloys. However, the bending tests showed a lack of ductility.

Bimodal microstructures were obtained in various types of metallic and composite materials after consolidation (SPS or HIP). Grain structures composed of ultrafined grains with coarser grains enhance ductility when compared to monomodal nanostructured materials [23–27]. Srinivasarao et al. [28] tailored the grain size distribution to obtain an excellent compromise between tensile strength and elongation with a milled iron powder consolidated by Spark Plasma Sintering. Other metallic materials such as Fe-Mo [29], Mg-Mn-Zr [30] showed similar properties. The origin of these complex microstructures is still unclear. The bimodal microstructure may result from heterogenous secondary recrystallization of some grains at the expense of others. This could be due to strain-induced boundary migration due to heterogenous plastic deformation upon milling process, combined with preferential pinning of some grain boundaries by fine and dense particles [23,31]. Regardless, the influence of such heterogenous microstructure on the mechanical properties is not straightforward, since the contribution of grain size mostly deviates from classic Hall–Petch hardening [32].

* Corresponding author.
E-mail address: damien.fabregue@insa-lyon.fr (D. Fabrègue).

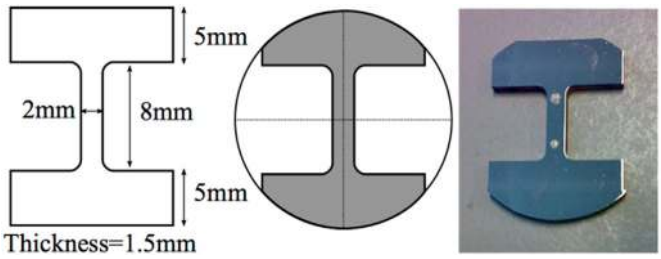

Fig. 1. Machining and tensile specimen dimension.

This study aims at investigating the influence of heterogenous ultra fine grained microstructure on the tensile properties of ferritic steels. To do so, the effect of milling and oxide dispersion on the formation of ultrafine grained steels was quantified. The consolidation of three model powders: atomized, milled and mechanically alloyed with oxides was performed in order to obtain various microstructures and resulting tensile behaviors. The comparison between the atomized and the milled powders allowed to quantify the effect of cold work on the microstructure. On the other hand, the milled material with and without oxides showed the influence of the precipitation state on the microstructure and the mechanical properties. The influence of processing and microstructure on the mechanical properties is discussed. This study constitutes a research path for the comprehensive study of heterogeneously ultrafine grained materials with high tensile strength.

2. Powders and consolidation

Three powders were consolidated:

(a) Atomized Powder (further referred as AP): produced by using gas atomization process under argon atmosphere of a pre-alloyed smelted steel Fe−14Cr−1W. The based powder was produced by Aubert&Duval [14].
(b) Milled Powder (further referred as MP): the atomized powder (a) was milled using a high-energy attritor under an argon atmosphere for 10 h at 400 rpm, in order to obtain a nanostructured ferritic powder. Steel balls (440C) with 8 mm diameter were used and the ball-to-powder mass ratio was 15.
(c) Mechanically alloyed with oxides powder (further referred as ODS for Oxide Dispersion Strengthened): the atomized powder was milled with yttria (Y_2O_3) (0.3wt%) and TiH_2 powders in order to produce ODS ferritic steel by Mechanical Alloying (MA) under similar conditions as for powder MP.

The only difference between AP and MP is the milling and the only difference between MP and ODS is the addition of oxides

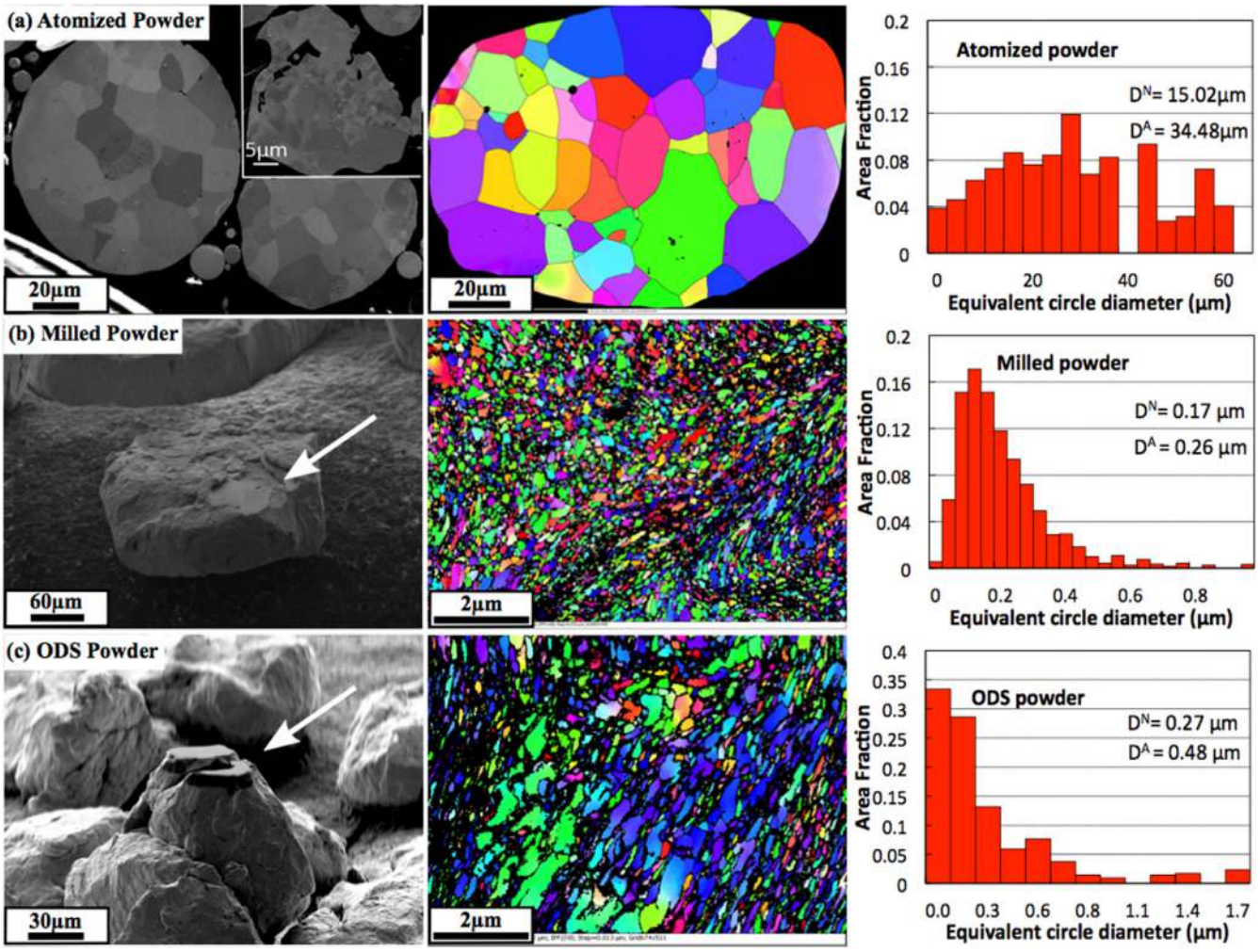

Fig. 2. Initial state of powders with for each specimen: Secondary Electron SEM image, EBSD orientation map and corresponding grain size distribution in area fraction. The inset in (a) shows small powder particle with smaller crystallite size. The cross-sectioned FIB areas were indicated by white arrows in (b) and (c).

during milling. The chemical composition of the three powders is given in Table 1.

The powders were then consolidated by SPS to form a dense cylindrical pellet of 20 mm diameter and 6 mm height. SPS device was a HP D 25 (FCT System, Germany). Sintering cycles were performed under 90 MPa average pressure, with a heating rate of 300 K min^{-1} up to the holding temperature for a soaking time of 5 min. The soaking temperature was chosen at 850, 950 and 1050°C. The cooling was ensured by direct contact with water-cooled punches, which induced a cooling rate of 200 K min^{-1}. The temperature was controlled by a thermocouple inserted in a hole in the graphite die close to the powder, which is the reference in this study.

In the following, consolidated materials will be denoted by the initials of the powder, followed by the SPS soaking temperature: *e.g.* MP850 means the milled powder consolidated at 850°C by SPS.

2.1. Experimental techniques

2.1.1. Machining

The SPS compacts were machined into either tensile specimen or metallographic cuts for density measurement, hardness testing and microstructure characterization. Furthermore, cross-sectioning and imaging on MP and ODS powders particles were performed using a FIB/SEM workstation combining a SIINT zeta FIB column (Seiko Instruments) with a Gemini column.

2.1.2. Density

Relative density of SPS compacts was measured using the Archimedes' principle where the mass of the sample emerged and immersed in water is measured using a very precise weighing scale.

2.1.3. Electronic microscopies

The microstructure was characterized by a scanning electron microscope (SEM) Zeiss Supra 55 VP with field-emission gun (FEG), using an Electron BackScatter System (EBSD) at 12 kV with a step size of 13–15 nm for milled powders and 40 nm for SPS compacts.

2.1.4. Mechanical properties

Hardness testing was performed on a Vickers indenter machine using a load of 300 g. For mechanical testing, dog bone tensile specimens had a gage length of 6 mm and a cross section of 1.5 × 2 mm^2. Mechanical tests were carried out at room temperature with a strain rate of 7.10^{-4} s^{-1} in a tensile machine Instron with a load cell of 30 kN and equipped with an optical extensometer measuring the increase in gage length between two painted dots (Fig. 1).

3. Results

3.1. Microstructure of the powders

The powder particles were machined by focused ion beam (FIB) and observed by SEM and EBSD. After atomization, the powder particles have fully ferritic structure with a mean diameter of 34.5 μm, as described in Fig. 2(a). Some pores are located both at "triple" grain junctions and within the grains. Microstructure heterogeneities can also be seen with disturbed and finer grains at some powder particles edges (Fig. 2(a, inset)). The two milled powders with and without yttria are nanostructured. However, the ODS powder particle investigated here contains larger grains up to 1 μm. More systematic investigation using classic imaging mode showed also homogenous and ultrafine grained zone (not shown here). Consequently, it will be considered that the two milled powders (MP and ODS) are both ultrafine-grained structure with slight difference in size. Influence of grain size is more relevant when comparing atomized and milled powders.

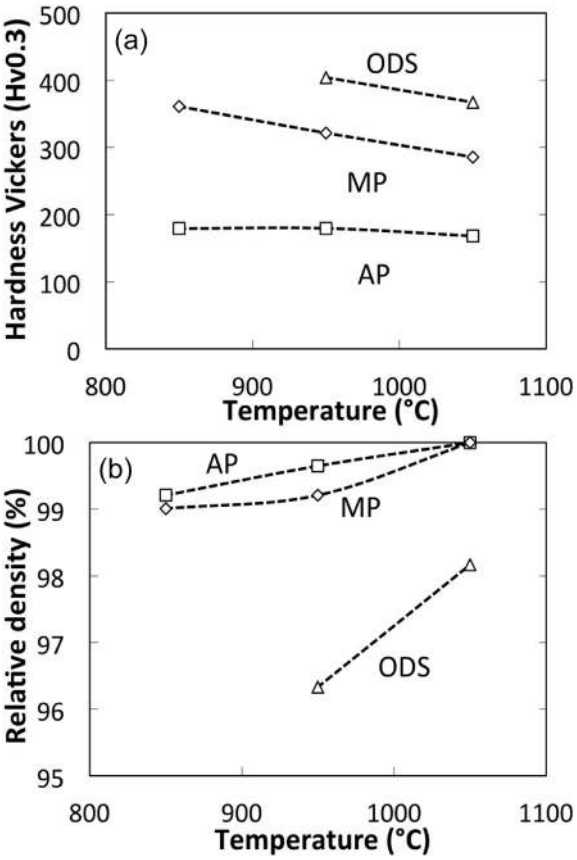

Fig. 3. Hardness and relative density of consolidated samples as a function of the SPS consolidation temperature.

3.2. Consolidation behavior

The three powders were then consolidated by SPS, as detailed in section 2. Table 2 lists the consolidation temperature, the relative density, the Vickers Hardness, the mean grain size for all SPS samples. Fig. 3 describes the hardness and relative density of consolidated samples. AP clearly has better densification behavior since it has higher relative density at the three temperatures compared to the two others. The hardness plateau with temperature expresses the relatively limited grain growth between 850 and 950 °C. Then, a more complex mechanism involving the formation of martensite occurs at 1050°C. The good densification behavior of AP compared to MP and ODS is related to both regular and spherical shape and lower particles hardness that facilitates plastic-induced rearrangement and densification. Indeed, the limit density up to which the material can plastically densify is related to the yield strength of the bulk materials. The latter is much lower in atomized than in nanostructured milled powders. Interestingly, the milled powder PM shows the equivalent densification behavior with a shift towards lower relative density at lower temperatures (850 and 950°C) and tends to be fully dense at 1050°C as well. MP samples clearly follow a continuous decrease of hardening with temperature, which tends to show that the gain in relative density is not sufficient to compensate the decrease of Hall–Petch strengthening. It can be concluded that at 1050°C, MP and AP are totally consolidated and MP has probably much finer microstructure that gives rise to an increase in hardness of more than 100 HV0.3.

ODS950 has much lower relative density than that of AP950 and MP950 consolidated at the same temperature. At 1050°C, the

difference diminishes but not enough (around 98%) to get full densification. Since the hardness is higher than both AP and MP, higher yield strength of powder particles is expected to reduce the ability to densify at moderate temperature. Then, diffusion mechanisms such as grain boundary sliding or volume diffusion are probably partial so that the full consolidation at short times cannot be achieved. This is even more emphasized at 850°C where ODS powder had remaining pores (not shown here). The evolution of hardness with temperature seems to vary with the nature of the powder. This point will be discussed in the next section, focused on the microstructural characterization.

3.3. Microstructure of consolidated materials

In order to understand the role of microstructure on the mechanical properties, a systematic investigation by SEM-FEG and EBSD was carried out on the 8 SPS compacts (porous ODS850 was excluded). EBSD maps are presented in Fig. 4. From these maps, grain size was determined based on either the arithmetical mean size D^N or the area-weighted mean size D^A:

$$D^N = \sum_{i=1}^{n} f_i^N \cdot D_i \quad (1)$$

$$D^A = \sum_{i=1}^{n} f_i^A \cdot D_i \quad (2)$$

where D_i is the diameter of grain i on the EBSD map, f_i^N and f_i^A are the number fraction and area fraction of size class i determined by EBSD. One key result is the quite constant Grain Size Distribution (GSD) between the as-atomized powder (cf. Fig. 2(a)) and AP850 (Fig. 5). Even if the GSD measured on the AP may not be representative enough and most likely overestimated, the mean diameter (D^A) was around 30 μm, which is equivalent to that of the AP850 sample. This demonstrates the limited grain growth at this temperature. Grain growth is also very slow at 950°C but drastically increases at 1050°C where the mean grain size reaches 186 μm. When focusing on interparticles boundaries, one can notice blocks of finer grains with a diameter below 10 μm. This can be interpreted by the formation of martensite blocks between ferrite grains (Fig. 4(c)). This martensite may nucleate from either local carbon-rich zones or scarcely dispersed inclusion, such as sulfites [33]. These blocks were also observed in the SPSed milled powder but not in the ODS powder. This can be explained by the ferrite-stabilizing effect of both titanium and oxygen added in the ODS powder compared to the two others. Formation of low fraction of austenite was observed by neutron in situ study by Zhang et al. [31]. Concerning the hardness plateau observed in the atomized powder, it can be assumed that the formation of austenite and further martensite during cooling can harden the material sufficiently to compensate the strength loss due to significant grain growth. Milled powder undergoes abnormal growth between 950 and 1050 °C. MP does not contain high density of particles but can

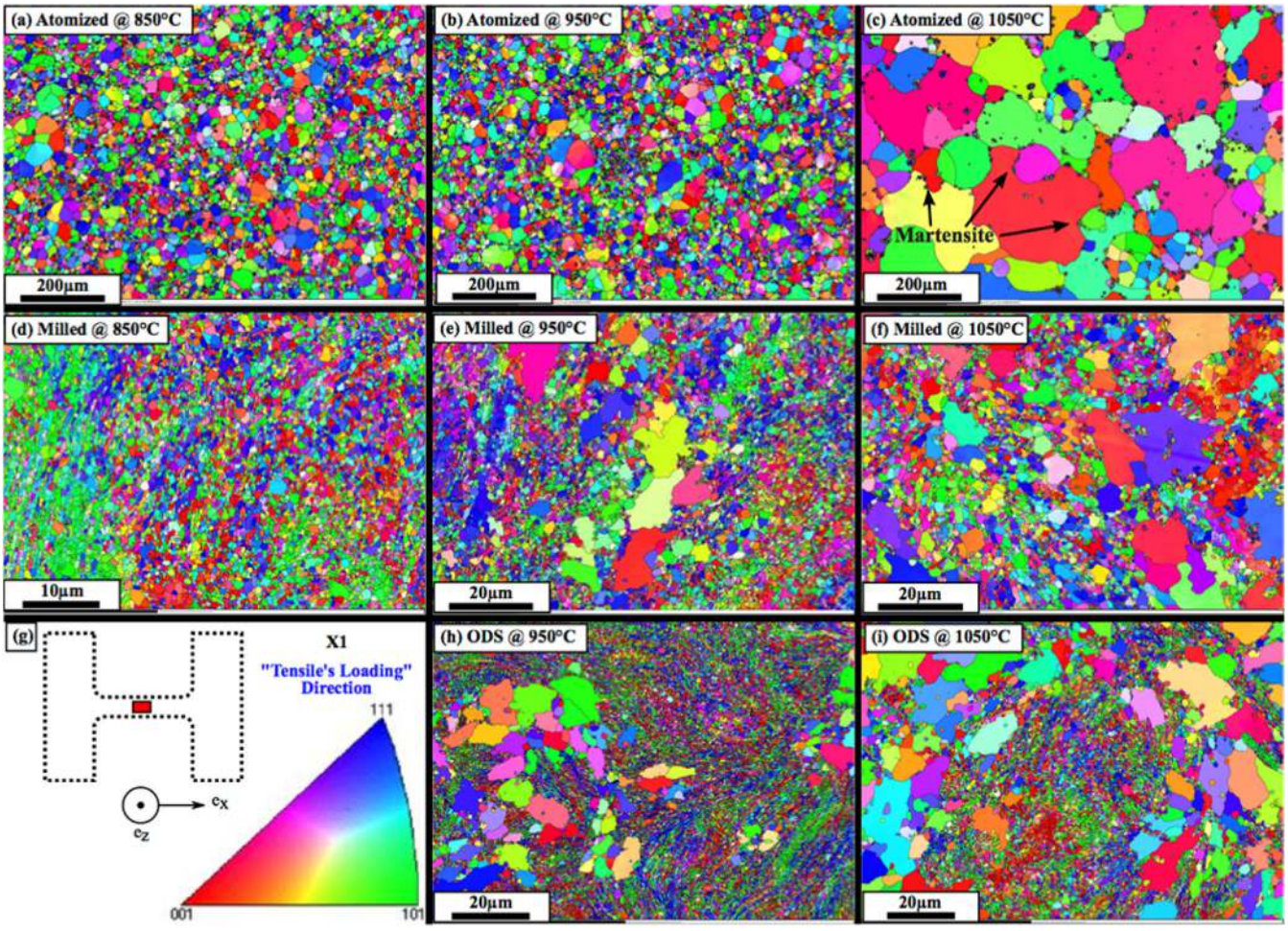

Fig. 4. EBSD map orientation of the 8 SPS compacts showing various metallurgical states. The microstructure was characterized on the gage length of the tensile specimen.

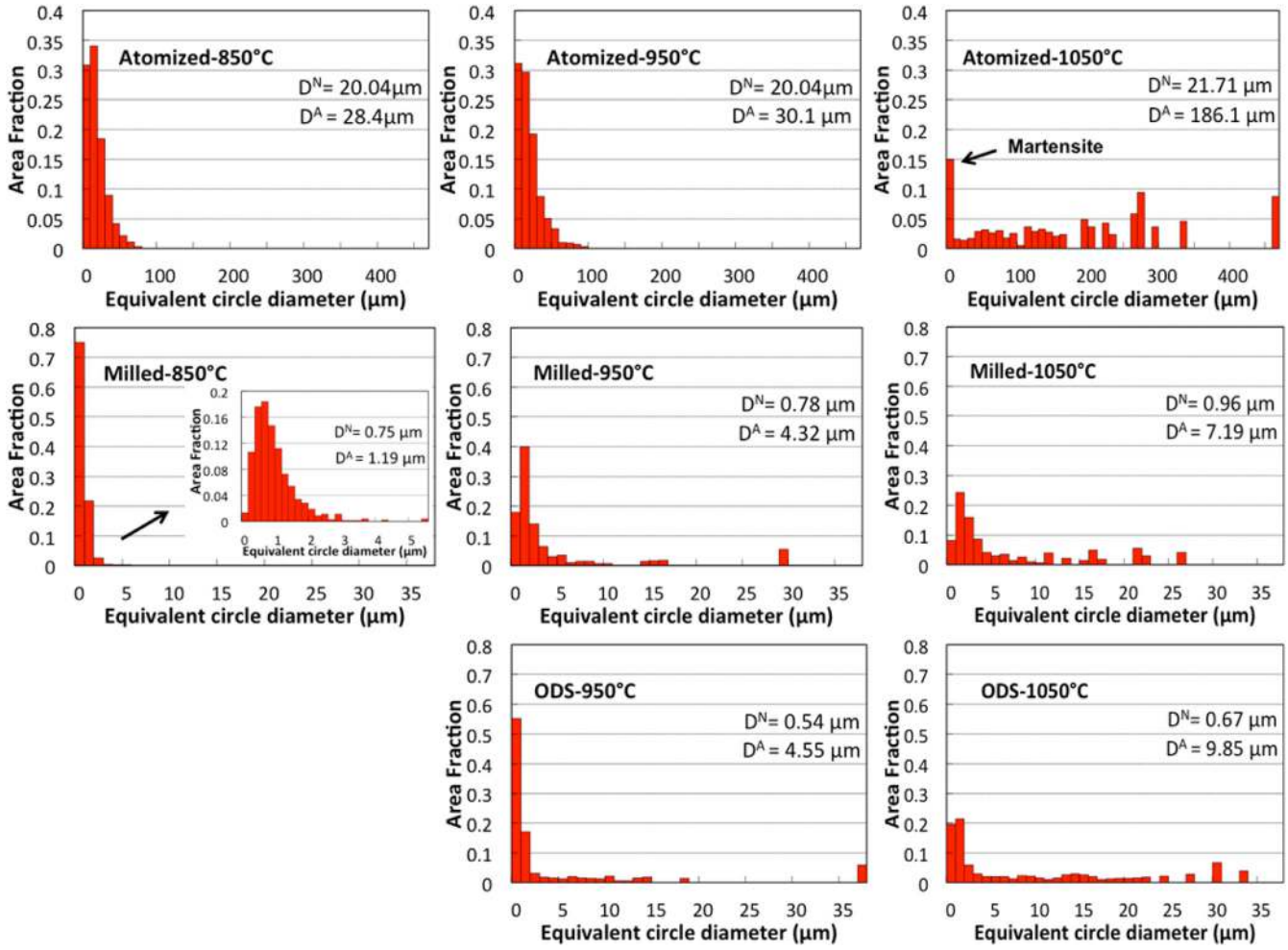

Fig. 5. Grain size distribution of the 8 metallurgical states with mean grain size D^N and D^A

contain carbides that may pin grain boundaries [24]. Even if this could lead to abnormal growth, the main cause of this bimodal microstructure is most likely heterogenous stored energy after milling. The driving force for Strain-Induced Boundary Migration (SIBM) is high enough to induce abnormal growth of selected grains at the expense of more deformed ones. This was demonstrated on milled ferritic powders consolidated by either spark plasma sintering or hot isostatic pressing [14]. This bimodal microstructure consists of both ultrafined grains with a mean diameter of 750 nm and coarse grains with a diameter up to 30 µm. Increasing the temperature gives similar microstructure, even if the UFG to coarse grains ratio decreases. Although it is not shown here, martensite blocks were also scarcely observed within the MP950 and MP1050. ODS950 and ODS1050 microstructures are also heterogenous, with similar grain size than that of oxide-free consolidated powders. This shows limited effect of oxide dispersion on the appearance of abnormal grains. This demonstrates that regardless the precipitation state, SIBM plays a significant role on the onset of abnormal grain growth. Also, within the studied temperature range and SPS process time, the bimodal microstructure seems to be stable.

3.4. Tensile properties

The tensile properties of all samples exhibit a large range of strength (with ultimate tensile strength of 1215 MPa for the MP850 and of 563 MPa for the AP1050) and of ductility (from 2 % to 33 %) for the same chemical composition (Fig. 7 and Table 3). AP samples show limited variation in both strength and elongation.

As shown, small martensite blocks may compensate the decrease of tensile strength due to grain growth. However, the Hall–Petch hardening seems to be very moderate in coarse-grained ferrite. AP samples have also quite constant uniform elongation, showing a moderate effect of grain size on ductility for homogenous coarse-grained ferrite. The consolidated milled powders have much higher strength (Fig. 7(b)) which cannot be uniquely explained by the Hall–Petch effect, as discussed in section 4. The ODS950 sample shows negligible plastic deformation. As shown before, it has remaining porosity that is likely detrimental to damage resistance.

Fractographic examinations were performed on the broken specimen to investigate the damaging behavior of the samples (Fig. 8). The necking-induced area reduction was measured on each sample and reported in Fig. 6. The area reduction of the three AP samples slightly increases from 60 to 68.3 % for AP850 and AP1050, respectively (Fig. 8(a–c)). They all exhibit ductile damage mode with numerous dimpled features. This shows the benefits of large grains that enhance the ductility. MP850 and MP950 show mixed ductile and intergranular damage mode whereas MP1050 sample has full ductile behavior. In this sample, the size and the geometry of the dimpled features are bimodal, which seems to be related to the bimodal grain structure observed by EBSD.

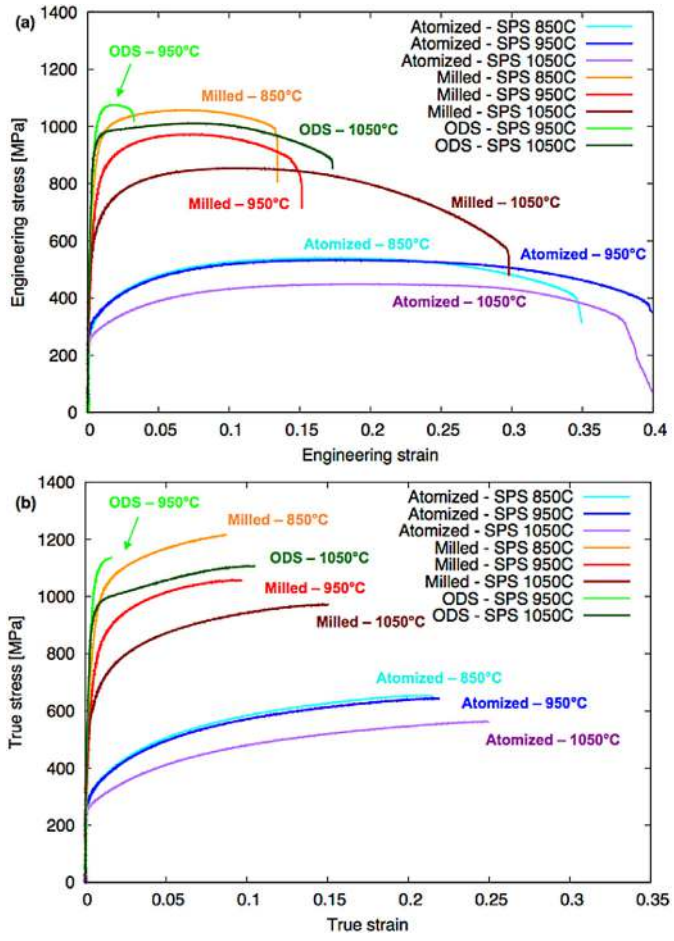

Fig. 6. Room temperature tensile behaviour of the consolidated samples: (a) Engineering Stress up to fracture and (b) True Stress.

ODS950 behavior undergoes the clear influence of remaining pores after consolidation (Fig. 8(g)). However, dimpled features are also observed, which demonstrates that porosity is not fully detrimental to plastic deformation. ODS1050 shows similar behavior to MP1050 with bimodal dimpled features most likely related to the bimodal grain structure. MP1050 has the same area reduction as that of coarse-grained AP1050 (Fig. 6), which demonstrates that large grains significantly boost the ability to accumulate plasticity. It can be concluded that the bimodal grain structure.

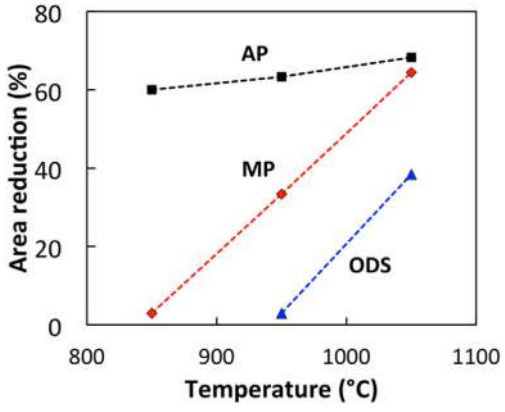

Fig. 7. Area reduction evolution as a function of consolidation temperature measured for each specimen.

4. Yield strength modeling

The yield strength of a metallic material is due to many microstructural contributions. One can summarize the strengthening mechanisms as follows [34,35]:

$$\sigma_{YS} = \sigma_0 + \sigma_{ss} + \sigma_{HP} + \sqrt{\sigma_{dis}^2 + \sigma_{ppt}^2} \tag{3}$$

where σ_0 is the Peierls-Nabarro friction stress in pure iron, which is needed for a dislocation to move into an atomic plane [36]. Based on Alinger's thesis [37], Hin et al. chose a value of 125 MPA in a simple strengthening model [38]. The strengthening contribution due to solid solution σ_{ss} is classically used for fcc materials with the following form:

$$\sigma_{ss} = \sum_i k_i \cdot X_i^Z \tag{4}$$

where X_i is the mass or atomic fraction and k_i a hardening constant of the element *i*. Actually, the original model by Mott and Nabarro dealt with the solute concentration rather than the mass fraction since there is no reason that the atomic weight plays on role on the hardening efficiency [39]. However, in the recent literature, the hardening constants k_i are calculated using this model. Whereas $z = 2/3$ is suitable for fcc materials like aluminum alloys [40,41], $z = 3/4$ for substitutional solid solution (Cr,W) [42–44] and $z = 1/2$ for interstitial elements (N,C) [45–47] are more suitable in bcc alloys.[1]

The grain size contribution σ_{HP} is referred to the Hall–Petch effect. This expresses the influence of grain boundaries on dislocations behaviour. Indeed, dislocations are gradually stacked at grain boundaries and form pile-ups until they reach the threshold-stress to pass into the next grain. This is given by:

$$\sigma_{HP} = \frac{k_{hp}}{\sqrt{D}} \tag{5}$$

where $k_{hp} = 0.2\mu\sqrt{b}$ [48], where μ and b are the shear modulus and the Burgers vector respectively, and D is the mean grain size. For homogenous ultrafine grained ferritic steels, Takaki et al. determined $k_{hp} = 0.6$ MPa$\cdot\sqrt{m}$ [49].

In addition to the two aforementioned contributions, two major mechanisms take part to the strengthening of ODS steels. Dislocation forest hardening σ_{dis} takes into account the interaction between existing dislocations (before mechanical testing, inherited from thermo-mechanical processing in non-fully recrystallized steels) and dislocations propagating during mechanical testing. This contribution is given by:

$$\sigma_{dis} = M\alpha\mu b\sqrt{\rho} \tag{6}$$

where M is the Taylor factor that depends on the crystallographic structure and the texture of the material, α a numerical constant which equals to 0.38 in ferrite [50], ρ the dislocation density.

Finally, the precipitation hardening can be quantified thanks to the Ashby–Orowan equation [51]:

$$\sigma_{ppt} = 0.84 \cdot \frac{1.2M\mu b}{2\pi\,\lambda_p} ln\left(\frac{\sqrt{2/3}\cdot r_p}{2b}\right) \tag{7}$$

where $\lambda_p = \left[1.25\sqrt{\frac{2\pi}{3f_p}} - 2\sqrt{\frac{2}{3}}\right] r_p$ is the mean distance between

[1] z tends to $z = 1/3$ in martensite [46].

Table 1
Chemical composition (wt%) and samples ID of the three powders measured by electron microprobe analysis. Oxygen contamination has probably occurred for AP and MP despite the precautions taken.

Element (wt%)	Fe	Cr	W	Si	Mn	Y	O	Ti
Atomized powder – AP	Bal.	14.6	0.99	0.3	0.3	/	Not measured	/
Milled powder – MP	Bal.	14.5	1.01	0.3	0.3	/	Not measured	/
Milled powder with oxide – ODS	Bal.	14.5	1.01	0.3	0.3	0.16	0.15	0.32

particules, r_p and f_p the precipitates mean radius and fraction [52]. This kind of model was previously applied on either HIPed or extruded steels [48,53,54]. Also, DiDomizio et al. and Kim et al. applied a full quadratic summation of the strengthening contributions in ODS ferritic steels [55,56]. Kim et al. showed that a linear superposition model was less relevant to predict the yield strength. The quadratic model takes into account the high probability of interacting mechanisms that are active in NFAs. As used in the current work, they also showed that a dispersed barrier model for precipitation hardening can be reliable to catch the strengthening mechanism of nano-oxides in ODS steels.

Various microstructural features were obtained by SPS, allowing to study the influence of each microstructural parameter at one time. This model was applied on all investigated samples consolidated by SPS and compared to experimental yield strengths (Fig. 9).

Consolidated AP samples allowed the solid solution, Hall–Petch and dislocation forest strengthening to be validated thanks to the experimental values (Table 4).

A dislocation density of fully recrystallized ferrite was chosen for the AP samples: 10^{13} m^{-2}

Dislocation densities of MP850, MP950 and MP1050 and ODS950 and ODS1050 samples were set at 5, 3 and 1×10^{14} m^{-2} and 3 and 1×10^{14} m^{-2} according to Synchrotron X-Ray diffraction study [57]. In the mentioned study, the milled powders were annealed up to 1100 °C and the dislocation density was determined using the peak broadening theory.

Precipitation hardening can be overestimated since the fraction of by-passed particles was not accurately determined. The precipitation hardening calculated from the small-angle neutron scattering (SANS) data reported in Ref. [14] ($r_p = 1.6$ nm and $f_p \approx 1\%$) accurately predicts the yield strength. These values are independent from the consolidation temperatures since the precipitation can form from 800°C [58] and exhibit extreme thermal stability up to 1100°C [59], the precipitates mean radius and fraction was considered constant for the two materials sintered at 950°C and 1050°C.

This contribution is lower than the precipitation contribution reported in other ODS steels tested at room temperature [60]. The few data available on the nanoscale characterization of particles in ODS steels processed by SPS indicate particles with a diameter between 5 nm [61–63] for the smallest particles up to 140 nm for the largest ones [64]. However, in ODS steels processed by SPS, the dislocation forest hardening is higher than in conventional ODS steels because recovery and recrystallization are limited during SPS compared to longer processes. The dislocation forest is thus quite significant, which justifies the tensile strength of the consolidated milled powder with no oxide strengthening.

The model using the arithmetical mean grain size is in better agreement than that with the volume-weighted grain size (Fig. 9), as it was already observed in ferritic grains [32]. In the case of heterogeneously grained material, such as bimodal structured steel, one can question why the arithmetic mean grain size is reliable. For that, a more specific study with using model materials would be of interest.

The strength difference between atomized and milled consolidated powders is due to both dislocation density and grain refinement. Hall–Petch effect is the most effective on M850 where most of nano-sized to ultrafine grains was retained in the consolidated sample. M950 and M1050 have tensile strength quite similar to the predicted values. Since no precipitation hardening was taken into account in these samples, one can estimate that coarse precipitates such as carbides may participate to strengthening. This simple model also reproduces the higher tensile strength of ODS steels compared to oxide-free milled steels. However, one should keep in mind that ODS950 has poor ductility due to remaining porosity (Fig. 7). ODS1050 has both good tensile strength and ductility, which can be interpreted by the combination of:

(i) bimodal microstructure that brings grain boundary hardening thanks to ultrafine grains and work-hardening potential thanks to coarse grains
(ii) additional strengthening thanks to the fine and dense oxides precipitation, which brings to ODS1050 higher strength than that of the M1050 for instance.

Table 2
Consolidation temperature, relative density, Vickers hardness, mean grain size from Equation (1) and Equation (2) for all SPS samples.

Initial powder	Ref.	T (°C)	ρ_r (%)	HV0.3	D^N(μm)	D^A (μm)
AP	AP850	850	99.2	179	20.04	28.4
	AP950	950	99.6	179	20.04	30.1
	AP1050	1050	100	168	21.71	186.1
MP	MP850	850	99	361	0.75	1.19
	MP950	950	99.2	321	0.78	4.32
	MP1050	1050	100	285	0.96	7.19
ODS	ODS950	950	96.3	404	0.54	4.55
	ODS1050	1050	98.1	367	0.67	9.85

Table 3
Mechanical properties of all consolidated samples.

Initial powder	Ref.	T_{SPS} (°C)	HV0.3	$R_{P0.2}$ (MPa)	UTS (MPa)	Area reduction coefficient (%)
AP	AP850	850	179	302	653	60
	AP950	950	179	292	643	63.6
	AP1050	1050	168	262	563	68.3
MP	MP850	850	361	862	1215	2.9
	MP950	950	321	791	1065	33.4
	MP1050	1050	285	610	972	64.4
ODS	ODS950	950	404	1064	1135	2.9
	ODS1050	1050	367	950	1106	38.4

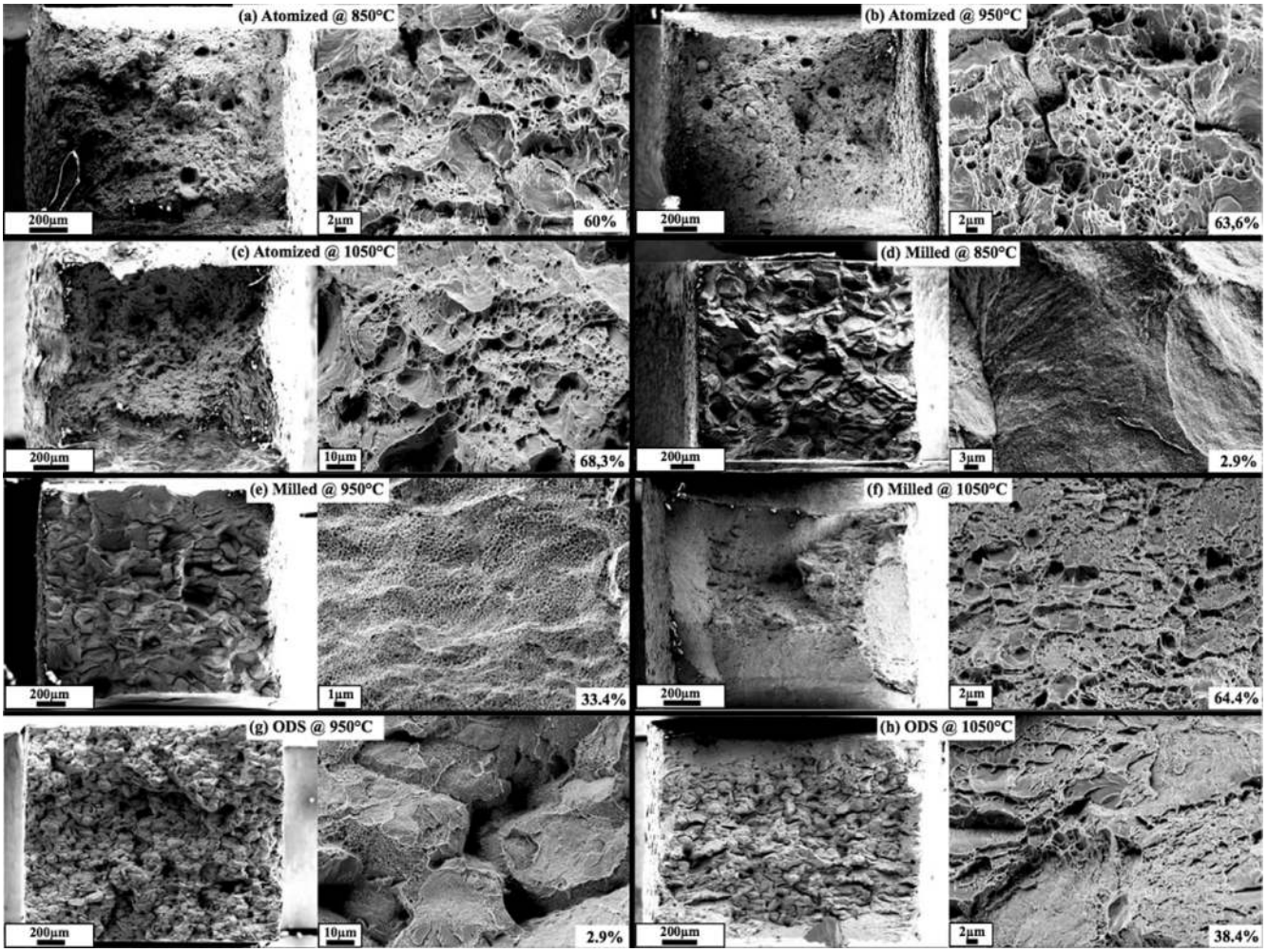

Fig. 8. SEM characterization of the broken specimen. The area reduction coefficient is given for each sample participates to the accumulation of plastic deformation, which results in bimodal dimpled features observed at the surface of the broken specimen. Also, remaining pores seen at the surface of the sample ODS950 explains the limited plastic deformation of the sample. This confirms that for ODS powder, a higher consolidation temperature is needed to achieve sufficient ductility.

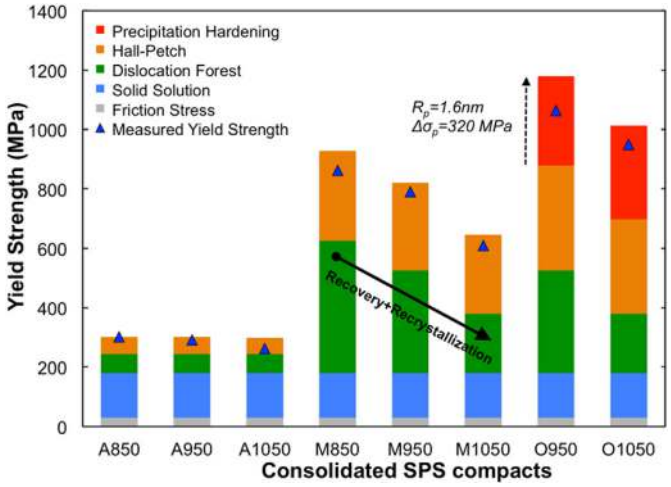

Fig. 9. Calculated yield strength using strengthening model from Equation (3). The Hall−Petch contribution was calculated using arithmetical mean grain size D^N.

5. Conclusion

Spark Plasma Sintering was used to compact three types of powders: (i) atomized, (ii) atomized + milled, (iii) atomized + milled with oxides. Compaction was performed at various temperatures ranging from 850 to 1050°C.

Whereas atomized powder exhibited rather large grains, milled powders display nano-grained structure with a bimodal grain size distribution for high temperature compactions.

Table 4
At the opposite, the constant microstructure parameters (HV,ρ,r_p and f_p) used for the strengthening model of all consolidated samples.

Parameters	Values	Ref.
σ_0 (MPa)	30	[45]
$k_{Cr}\cdot$[MPa/at%$^{3/4}$]	9.95	[42,45,53]
$k_W\cdot$[MPa/at%$^{3/4}$]	75.79	[42,45,53]
$k_C\cdot$[MPa/at%$^{1/2}$]	1122.5	[46]
$k_{hp}\cdot$[MPa.$\sqrt{m}$]	0.26	[48]
α	0.38	[50]
M	2.77	[50]
μ [GPa]	83	
b [nm]	0.248	
r_p [nm]	1.6	[14,65,66]
f_p [%]	1	[14]

These bimodal grain size distributions are believed to provide particular mechanical properties: *i.e.* high yield stress (probably due to the small grains) combined with high ductility (probably due to the large grains). Moreover, fracture analysis proved that all sample experienced ductile failure.

Finally, a yield stress model based on the contribution of solute elements, grain size, forest dislocations and precipitates allowed an accurate prediction of yield stress for all powder and compaction temperatures.

However, a complete physical variables-based model is needed to understand the role of second-phase particles and grain boundaries on the work-hardening behaviour [67] [41]. To do so, cyclic tests on ODS ferritic steels would permit to determine work-hardening fitting parameters and further quantify the effect of microstructure and precipitation on ductility [68] [69].

Acknowledgments

X. Boulnat was supported by the European Community within the FP7 Project MATTER and in the frame of a tripartite agreement between the CEA, AREVA NP, and EDF. D. Bardel is acknowledged for discussion on the work-hardening behaviour.

References

[1] R. Song, D. Ponge, D. Raabe, J.G. Speer, D.K. Matlock, Mater. Sci. Eng. A 441 (2006) 1.
[2] M.M. Cisneros, E. Valdés, D. Vázquez, H.F. López, H. Mancha, G. Mendoza, M. Méndez, Metall. Mater. Trans. A 33 (2002) 2139.
[3] K. Gonsalves, Nanostructured Steel Alloy 5 (589) (1996) 011.
[4] S. Ukai, M. Harada, H. Okada, M. Inoue, S. Nomura, S. Shikakura, T. Nishida, M. Fujiwara, K. Asabe, J. Nucl. Mater. 204 (1993) 74.
[5] S. Ukai, M. Fujiwara, J. Nucl. Mater. 307–311 (2002) 749.
[6] R.L. Klueh, D.S. Gelles, S. Jitsukawa, A. Kimura, G.R. Odette, B. van der Schaaf, J. Nucl. Mater. 307–311 (2002) 455.
[7] P. Dubuisson, Y. DeCarlan, V. Garat, M. Blat, J. Nucl. Mater. 428 (2012) 6.
[8] Y. de Carlan, J.-L. Bechade, P. Dubuisson, J.-L. Seran, P. Billot, A. Bougault, T. Cozzika, S. Doriot, D. Hamon, J. Henry, M. Ratti, N. Lochet, D. Nunes, P. Olier, T. Leblond, M.H. Mathon, J. Nucl. Mater. 386–388 (2009) 430.
[9] S. Saroja, A. Dasgupta, R. Divakar, S. Raju, E. Mohandas, M. Vijayalakshmi, K.B.S. Rao, B. Raj, J. Nucl. Mater. 409 (2011) 131.
[10] M.A. Auger, V. de Castro, T. Leguey, A. Muñoz, R. Pareja, J. Nucl. Mater. 436 (2013) 68.
[11] M. Wang, Z. Zhou, H. Sun, H. Hu, S. Li, Mater. Sci. Eng. A 559 (2013) 287.
[12] Z. Oksiuta, N. Baluc, J. Nucl. Mater. 386–388 (2009) 426.
[13] N.J. Cunningham, Study of the Structure, Composition, and Stability of Y-Ti-O Nm–Scale Features in Nano-structured Ferritic Alloys, University of California, Santa Barbara, 2012.
[14] X. Boulnat, M. Perez, D. Fabrègue, T. Douillard, M.H. Mathon, Y. DeCarlan, Metall. Mater. Trans. A 45A (2014) 1485.
[15] P. Angerer, E. Neubauer, L.G. Yu, K.A. Khor, Int. J. Refract. Met. Hard Mater. 25 (2007) 280.
[16] I. Lonardelli, M. Bortolotti, W. van Beek, L. Girardini, M. Zadra, H.K.D.H. Bhadeshia, Mater. Sci. Eng. A 555 (2012) 139.
[17] G. Ji, T. Grosdidier, N. Bozzolo, S. Launois, Intermetallics 15 (2007) 108.
[18] D. Fabrègue, J. Piallat, E. Maire, Y. Jorand, V. Massardier-Jourdan, G. Bonnefont, Powder Metall. 55 (2012) 76.
[19] R. Orrù, R. Licheri, A.M. Locci, A. Cincotti, G. Cao, Mater. Sci. Eng. R. Reports 63 (2009) 127.
[20] W.M. Guo, Z.G. Yang, G.J. Zhang, Int. J. Refract. Met. Hard Mater. 29 (2011) 452.
[21] B. Mouawad, M. Soueidan, D. Fabrègue, C. Buttay, V. Bley, B. Allard, H. Morel, Metall. Mater. Trans. A 43 (2012) 3402.
[22] T. Grosdidier, G. Ji, S. Launois, Scr. Mater. 57 (2007) 525.
[23] X. Boulnat, D. Fabrègue, M. Perez, M.H. Mathon, Y. Decarlan, Metall. Mater. Trans. A 44 (2013) 2461.
[24] C. Menapace, I. Lonardelli, M. Tait, A. Molinari, Mater. Sci. Eng. A 517 (2009) 1.
[25] Y. Wang, M. Chen, F. Zhou, E. Ma, Nature 419 (2002) 912.
[26] C.C. Koch, Scr. Mater. 49 (2003) 657.
[27] A.K. Mukherjee, Mater. Sci. Eng. A 322 (2002) 1.
[28] B. Srinivasarao, K. Oh-ishi, T. Ohkubo, K. Hono, Acta Mater. 57 (2009) 3277.
[29] M. Cabibbo, C. Paternoster, R. Cecchini, A. Fabrizi, A. Molinari, S. Libardi, M. Zadra, Mater. Sci. Eng. A 496 (2008) 121.
[30] W.J. Kim, I.K. Moon, S.H. Han, Mater. Sci. Eng. A 538 (2012) 374.
[31] H. Zhang, M.J. Gorley, K.B. Chong, M.E. Fitzpatrick, S.G. Roberts, P.S. Grant, J. Alloys Compd. 582 (2014) 769.
[32] H. Qiu, R. Ito, K. Hiraoka, Mater. Sci. Eng. A 435–436 (2006) 648.
[33] D.S. Sarma, A.V. Karasev, P.G. Jönsson, ISIJ Int. 49 (2009) 1063.
[34] A. Deschamps, Y. Brechet, Acta Mater. 47 (1998) 293.
[35] A. de Vaucorbeil, W.J. Poole, C.W. Sinclair, Mater. Sci. Eng. A 582 (2013) 147.
[36] G. Lu, Handbook of Materials Modeling, Springer, Netherlands, 2005.
[37] M.J. Alinger, On the Formation and Stability of Nanometer Scale Precipitates in Ferritic Alloys during Processing and High Temperature Service, University of California Santa Barbara, 2004.
[38] C. Hin, B.D. Wirth, J. Nucl. Mater. 402 (2010) 30.
[39] J. Friedel, Dislocations, Addison-Wesley, 1964.
[40] U.F. Kocks, H. Mecking, Prog. Mater. Sci. 48 (2003) 171.
[41] D. Bardel, M. Perez, D. Nelias, A. Deschamps, C.R. Hutchinson, D. Maisonnette, T. Chaise, J. Garnier, F. Bourlier, Acta Mater. 62 (2014) 129.
[42] C.E. Lacy, M. Gensamer, Trans. Am. Soc. Met. 32 (1944) 85.
[43] M. Praud, Plasticité D'alliages Renforcés Par Nano-précipitation, Université de Toulouse, 2012.
[44] P. Susila, D. Sturm, M. Heilmaier, B.S. Murty, V.S. Sarma, Mater. Sci. Eng. A 528 (2011) 4579.
[45] Q. Li, Mater. Sci. Eng. A 361 (2003) 385.
[46] C.H. Young, H.K.D.H. Bhadeshia, Mater. Sci. Technol. 10 (1994) 209.
[47] C.H. Young, H.K.D.H. Bhadeshia, J. Phys. IV Fr. 05 (1995) C8.
[48] M. Ratti, Développement de Nouvelles Nuances D'aciers Ferritiques-Martensitiques Pour Le Gainage D'éléments Combustibles Des Réacteurs À Neutrons Rapides Au Sodium, Institut Polytechnique de Grenoble, 2010.
[49] S. Takaki, K. Kawasaki, Y. Kimura, J. Mater. Process. Technol. 117 (2001) 359.
[50] M. Perrier, Etude de La Relation Entre La Microstructure et Les Propriétés Mécaniques D'un Acier Durci Par Précipitation Intermétallique Intense: Le Fer-Silicium-Titane, Universite de Grenoble, 2011.
[51] M.F. Ashby, Philos. Mag. 14 (1966) 1157.
[52] J.W. Martin, Micromechanisms in Particle-hardened Alloys, in: Cambridge Solid State Science Series, 1980.
[53] M. Couvrat, Fabrication D'aciers ODS À Haute Performance: Relation Procédé Microstructure Propriétés Mécaniques, Université de Rennes 1, 2013.
[54] S.Y. Zhong, Effet de La Composition Chimique Sur La Cinétique de Coalescence Des Oxydes Dans Les Aciers Renforcés ODS Fe-14%Cr, Université Paris-Sud 11, 2012.
[55] R. DiDomizio, S. Huang, L. Dial, J. Ilavsky, M. Larsen, Metall. Mater. Trans. A 45 (2014) 5409.
[56] J.H. Kim, T.S. Byun, D.T. Hoelzer, C.H. Park, J.T. Yeom, J.K. Hong, Mater. Sci. Eng. A 559 (2013) 111.
[57] N. Sallez, X. Boulnat, A. Borbély, J.L. Béchade, D. Fabrègue, M. Perez, Y. de Carlan, L. Hennet, C. Mocuta, D. Thiaudière, Y. Bréchet, Acta Mater. 87 (2015) 377.
[58] C.A. Williams, P. Unifantowicz, N. Baluc, G.D.W. Smith, E.A. Marquis, Acta Mater. 61 (2013) 2219.
[59] N. Cunningham, Y. Wu, D. Klingensmith, G.R. Odette, Mater. Sci. Eng. A 613 (2014) 296.
[60] A. Steckmeyer, M. Praud, B. Fournier, J. Malaplate, J. Garnier, J.L. Béchade, I. Tournié, A. Tancray, A. Bougault, P. Bonnaillie, J. Nucl. Mater. 405 (2010) 95.
[61] C. Heintze, F. Bergner, A. Ulbricht, M. Hernández-Mayoral, U. Keiderling, R. Lindau, T. Weissgärber, J. Nucl. Mater. 416 (2011) 35.
[62] C. Heintze, M. Hernández-Mayoral, A. Ulbricht, F. Bergner, A. Shariq, T. Weissgärber, H. Frielinghaus, J. Nucl. Mater. 428 (2012) 139.
[63] K.N. Allahar, J. Burns, B. Jaques, Y.Q. Wu, I. Charit, J. Cole, D.P. Butt, J. Nucl. Mater. 443 (2013) 256.
[64] Q.X. Sun, T. Zhang, X.P. Wang, Q.F. Fang, T. Hao, C.S. Liu, J. Nucl. Mater. 424 (2012) 279.
[65] M. Ratti, D. Leuvrey, M.H. Mathon, Y. de Carlan, J. Nucl. Mater. 386–388 (2009) 540.
[66] Y. Wu, E.M. Haney, N.J. Cunningham, G.R. Odette, Acta Mater. 60 (2012) 3456.
[67] Y. Estrin, Unified Const. Laws Plast. Deform, Academic Press, 1996, pp. 69–106.
[68] S. Ukai, S. Ohtsuka, J. Nucl. Mater. 367–370 (2007) 234.
[69] I. Kubena, B. Fournier, T. Kruml, J. Nucl. Mater. 424 (2012) 101.